



# Cryo-electron Microscopy Structure and Transport Mechanism of a Wall Teichoic Acid ABC Transporter

Li Chen,<sup>a</sup> Wen-Tao Hou,<sup>a</sup> Tao Fan,<sup>b</sup> Banghui Liu,<sup>a</sup> Ting Pan,<sup>a</sup> Yu-Hui Li,<sup>b</sup> Yong-Liang Jiang,<sup>a</sup> Wen Wen,<sup>a</sup> Zhi-Peng Chen,<sup>a</sup> Linfeng Sun,<sup>a,c</sup> Cong-Zhao Zhou,<sup>a</sup> Yuxing Chen<sup>a</sup>

<sup>a</sup>Hefei National Laboratory for Physical Sciences at the Microscale and School of Life Sciences, University of Science and Technology of China, Hefei, Anhui, China

<sup>b</sup>School of Chemistry and Materials Science, University of Science and Technology of China, Hefei, Anhui, China

<sup>c</sup>CAS Centre for Excellence in Molecular Cell Science, University of Science and Technology of China, Hefei, Anhui, China

Li Chen and Wen-Tao Hou contributed equally to this work. Author order was determined alphabetically.

**ABSTRACT** The wall teichoic acid (WTA) is a major cell wall component of Gram-positive bacteria, such as methicillin-resistant *Staphylococcus aureus* (MRSA), a common cause of fatal clinical infections in humans. Thus, the indispensable ABC transporter TarGH, which flips WTA from cytoplasm to extracellular space, becomes a promising target of anti-MRSA drugs. Here, we report the 3.9-Å cryo-electron microscopy (cryo-EM) structure of a 50% sequence-identical homolog of TarGH from *Alicyclobacillus herbarius* at an ATP-free and inward-facing conformation. Structural analysis combined with activity assays enables us to clearly decode the binding site and inhibitory mechanism of the anti-MRSA inhibitor Targocil, which targets TarGH. Moreover, we propose a “crankshaft conrod” mechanism utilized by TarGH, which can be applied to similar ABC transporters that translocate a rather big substrate through relatively subtle conformational changes. These findings provide a structural basis for the rational design and optimization of antibiotics against MRSA.

**IMPORTANCE** The wall teichoic acid (WTA) is a major component of cell wall and a pathogenic factor in methicillin-resistant *Staphylococcus aureus* (MRSA). The ABC transporter TarGH is indispensable for flipping WTA precursor from cytoplasm to the extracellular space, thus making it a promising drug target for anti-MRSA agents. The 3.9-Å cryo-EM structure of a TarGH homolog helps us to decode the binding site and inhibitory mechanism of a recently reported inhibitor, Targocil, and provides a structural platform for rational design and optimization of potential antibiotics. Moreover, we propose a “crankshaft conrod” mechanism to explain how a big substrate is translocated through subtle conformational changes of type II exporters. These findings advance our understanding of anti-MRSA drug design and ABC transporters.

**KEYWORDS** cryo-EM, *Staphylococcus aureus*, inhibitors, wall teichoic acids, ABC transporters, MRSA, structure

Methicillin-resistant *Staphylococcus aureus* (MRSA) is a common clinical pathogen leading to difficult-to-treat, in many cases even fatal, infections in humans (1). Due to the abuse of antibiotics in recent decades, many MRSA strains are resistant to all β-lactams, even to the last-resort antibiotic vancomycin (2). Most of the present clinical β-lactam antibiotics target the peptidoglycan synthesis pathway (3). However, the emergence of various MRSA strains makes an urgent appeal to develop new antibiotics against enzymes controlling the biosynthesis of other cell wall components, such as wall teichoic acids and lipoteichoic acids (WTAs and LTAs, respectively).

WTAs are anionic glycopolymers attaching to the peptidoglycan of Gram-positive

**Citation** Chen L, Hou W-T, Fan T, Liu B, Pan T, Li Y-H, Jiang Y-L, Wen W, Chen Z-P, Sun L, Zhou C-Z, Chen Y. 2020. Cryo-electron microscopy structure and transport mechanism of a wall teichoic acid ABC transporter. *mBio* 11:e02749-19. <https://doi.org/10.1128/mBio.02749-19>.

**Invited Editor** Chris Whitfield, University of Guelph

**Editor** Nina R. Salama, Fred Hutchinson Cancer Research Center

**Copyright** © 2020 Chen et al. This is an open-access article distributed under the terms of the [Creative Commons Attribution 4.0 International license](https://creativecommons.org/licenses/by/4.0/).

Address correspondence to Linfeng Sun, sunlf17@ustc.edu.cn; Cong-Zhao Zhou, czz@ustc.edu.cn; or Yuxing Chen, cyxing@ustc.edu.cn.

**Received** 14 October 2019

**Accepted** 21 February 2020

**Published** 17 March 2020

bacteria (4) and are the key components that comprise up to 50% of the total mass of cell wall (5, 6). WTAs are crucial for cell division, biofilm formation, host colonization, and infection (1, 7). Some *S. aureus* strains have evolved a mechanism to escape hosts' immune systems via modifying their WTAs into altered structures that resist host lysozyme or corresponding antibodies (8, 9). Thus, the enzymes that control the rate-limiting steps of the WTA biosynthesis pathway become a pool of candidates for developing novel antibiotics against MRSA infections (10).

Undecaprenyl diphosphate (UND-PP) is a key lipid carrier for the biosynthesis of WTAs and a variety of other cell wall polysaccharide components, such as lipopolysaccharides (11), bacterial peptidoglycan (12), and capsular polysaccharides (13). However, linking to UND-PP is not sufficient *per se* for the sugar chain to pass the thermodynamic barrier of a lipid bilayer via free diffusion (14). Therefore, a group of dedicated flippases in the ATP-binding cassette (ABC) superfamily have been evolved. In *S. aureus*, ABC transporter TarGH is indispensable for the transmembrane flipping of WTA precursor, an *N*-acetylglucosamine (GlcNAc)-modified ribitol-phosphate (RboP) polymer covalently linked to the UND-PP moiety, out of the cell membrane (1, 10) (see Fig. S1 in the supplemental material). Aiming at TarGH as a potential target, a well-known inhibitor, Targocil, with a MIC of 0.3  $\mu$ M, was recently identified by Lee and coworkers (15). Moreover, random screening of the anti-Targocil *S. aureus* strains has identified a couple of putative Targocil binding residues on TarGH (16). However, the biochemical and structural evidence is absent.

The present structural knowledge on the ABC flippases that transport diverse UND-PP-linked substrates is limited to two structures. One is Pglk from human pathogen *Campylobacter jejuni*, which translocates intracellular UND-PP-GlcGalNAc<sub>5</sub>Bac out of the membrane for the *N*-glycosylation of bacterial surface proteins (17). The structure depicted a type I exporter that adopts a lateral access and "outward only" mechanism (18). Another is a type II exporter from *Aquifex aeolicus* (19, 20), termed Wzm-Wzt, the homolog of which in *Escherichia coli* O9a flips a UND-PP-linked intermediate into the periplasm for the synthesis of O antigens (11). Notably, the extra carbohydrate binding domain, which plays an important role in recognizing the sugar moiety of the substrate (21, 22), was deleted in the crystal structure, termed Wzm-WtzN. However, the structural and functional diversity of UND-PP-linked substrates make the transport mechanism of these ABC flippases poorly understood. Here, we determined the cryo-electron microscopy (cryo-EM) structure of *Alicyclobacillus herbarius* TarGH at 3.9 Å, which allowed us to gain more insights into the WTA transport driven by *S. aureus* TarGH and provided a structural platform for the rational design and further optimization of inhibitors of WTA flipping.

## RESULTS

**Overall structure of TarGH.** After systematic trials, we failed in overexpressing *S. aureus* TarGH; however, we succeeded in purifying the recombinant TarGH homolog from *A. herbarius* (see Fig. S3A in the supplemental material). As it shares an overall sequence identity of ~50%, it should be an ideal prototype of *S. aureus* TarGH (Fig. S2A and B). Using the cryo-electron microscopy (cryo-EM) technique, we solved the structure of *A. herbarius* TarGH at an overall resolution of 3.9 Å (Fig. 1A), with the catalytic residue Glu169 mutated to Gln. Analysis of the regional resolution showed that the core structure has a relatively high resolution of 3.6 Å, whereas the surface-exposed regions possess a rather lower resolution. In general, the nucleotide-binding domains (NBDs), which are encoded by the *tarH* gene, have a relatively lower resolution than the transmembrane domains (TMDs) encoded by the *tarG* gene.

In the absence of ATP, TarGH adopts an inward-open conformation (Fig. 1B). TarH/NBD possesses a classic NBD fold of ABC transporter, with an  $\alpha$ -helical subdomain and a RecA-like ATPase core subdomain. All conserved motifs, including Walker A and B, the ABC signature motif, could be clearly assigned in our structure. The distance between the hydroxyl groups of Ser64 on Walker A from one NBD and Ser146 on the

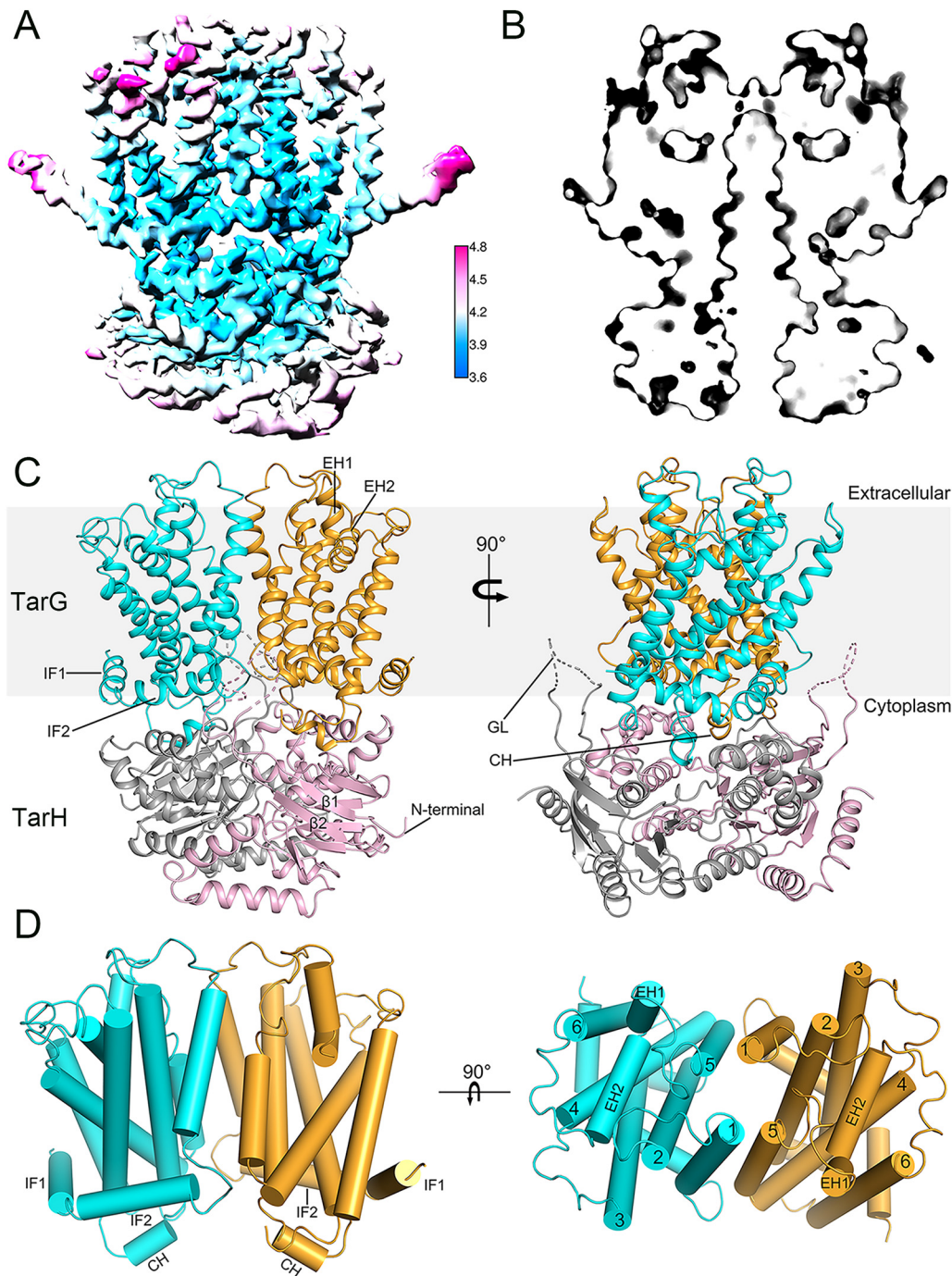


**FIG 1** Structure of TarGH (TarH<sub>E169Q</sub>) from *Alicyclobacillus herbarius*. (A) The local resolution map calculated using Relion. The overall resolution for the EM map is about 3.9 Å, while the local resolution for the core region reaches 3.6 Å. (B) TarGH is in an inward-facing conformation. A section view for the protein surface is shown here, indicating that the tunnel is closed at the extracellular side and accessible from the cytoplasm. (C) Overall structure of TarGH. TMDs encoded by *tarG* are shown in cyan and orange, and NBDs encoded by *tarH* are shown in gray and pink. (D) Structure of TMDs. The gate loop (GL), coupling helices (CHs), extracellular gate helices (EH1 and EH2), and interface helices (IF1 and IF2) are labeled. The TM helices are numbered sequentially.

signature motif from the other is about 6 Å, suggesting a resting state of TarGH ready for ATP binding.

Similar to other type II ABC exporters (23), the TMDs of TarGH consist of 6 + 6 transmembrane helices (TMs) without domain swapping (Fig. 1C and D). TM1 of one TMD packs against TM5 of the other, and vice versa, forming a total interface area of



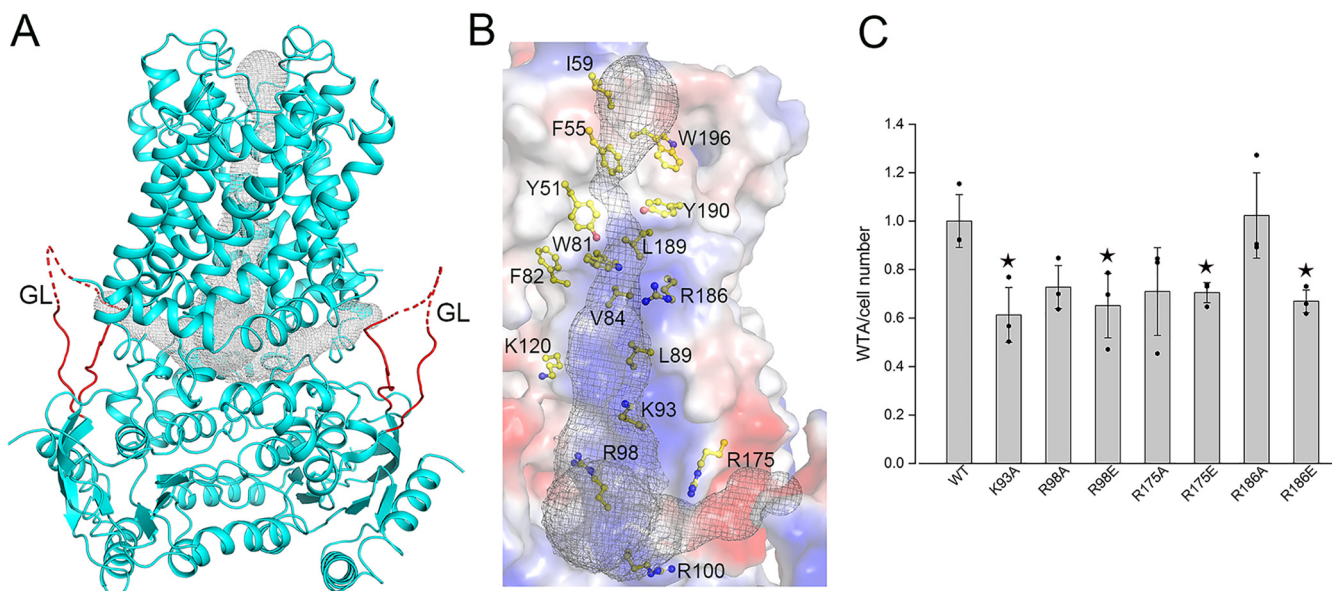


**FIG 2** The putative substrate tunnel. (A) Two L-shaped tunnels were simulated using the program Caver 3.0.1, as indicated by gray mesh. GLs close to the entrance are shown in red. (B) Hydrophobic residues surrounding the vertical path and positively charged residues located at the turn of the entrance are shown as sticks. (C) Quantification of WTA in *S. aureus* NCTC8325 transformed with pLI50-*tarG* and its mutants. At least three independent experiments were performed for each assay. The means and standard deviations were calculated, and the data are presented as means  $\pm$  standard deviations. Two results of three experiments in the wild-type (WT) group were overlapped due to similar values. Two-tailed Student's *t* test is used for the comparison of statistical significance. The *P* values <0.05, 0.01, and 0.001 are indicated with single, double, and triple stars, respectively.

1,110 Å<sup>2</sup>. We also found two reentrant helices between TM5 and TM6 that insert in the outer leaflet of membrane, termed extracellular helices EH1 and EH2 (Fig. 1C), like other type II exporters (19, 23, 24). In addition, each TMD is preceded by an extra amphipathic helix at the N terminus, compared to that in Wzm-WztN (19), sticking at the interface between the membrane and cytosol; thus, these are termed the interface helices IF1 and IF2 (Fig. 1C). Notably, this extra IF1 is conserved in most teichoic acid transporters (Fig. S2C). As in a typical ABC transporter, the conformational changes between TMDs and NBDs are also interconnected by the coupling helix (CHs), a short helix between TM2 and TM3. Each CH protrudes from the TMD and is embedded in a groove on the NBD at the same side without domain swapping. In addition, a flexible loop between  $\beta$ 1 and  $\beta$ 2 of the NBD extends toward the TMD, forming a putative substrate entrance on each side (Fig. 1C). Remarkably, the distal moiety of the corresponding loop in the Wzm-WztN structure, which is folded into a short  $\alpha$ -helix due to direct contacts with the TMD, was proposed to function as a gate of the substrate binding pocket and termed the gate helix (GH) (19). Accordingly, we propose that the flexible loop in our structure functions as a gate loop (GL).

**The putative substrate translocation tunnels.** Using the program Caver 3.0.1 (25), with the probe radius set to 1.1 Å, we simulated two back-to-back L-shaped substrate tunnels, each of which has a horizontal entrance along the membrane-cytosol interface and a vertical path through the cell membrane (Fig. 2A). The entrance starts at a putative gate, which is guarded by three loops, namely, GL, Loop<sub>IF2-TM1</sub>, and Loop<sub>TM4-TM5</sub>, and extends to the sharp turn of the L-shaped tunnel (Fig. 2A). The turn is surrounded by a line of positively charged residues, Lys93, Arg98, Arg100, Lys120, Arg175, and Arg186, whereas the transmembrane path is mainly composed of hydrophobic residues, such as Tyr51, Phe55, Trp81, Phe82, Val84, Leu89, Leu189, Tyr190, and Trp196 (Fig. 2B). Notably, this tunnel is complementary in charge to the structure of the UND-PP moiety, which has a lipid chain followed by two acidic phosphate groups (Fig. S6B).

In fact, a similar tunnel with a positively charged entrance followed by a hydrophobic path also exists in the structures of Pglk (18) and Wzm-WztN (19). Transport activity

assays proved that UND-PP-linked polysaccharides of various lengths could be recognized and exported by Pglk (18). In addition, complementary experiments indicated that the *Bacillus subtilis tagGH* gene could be replaced by *S. aureus tarGH*, without significant difference in the synthesis of WTA (16). It suggested that the UND-PP moiety, rather than the polysaccharide chain, determines the recognition and initiation of the entry of full-length substrate (16, 18, 26). We proposed that at the initial step of substrate binding, the diphosphate group of the UND-PP moiety guides the substrate binding to TarGH via specific interactions with the positively charged residues at the turn of the tunnel entrance. Notably, only a part of residues along the GL could be assigned to the electron density map in our structure (Fig. S5B), indicating its high flexibility and weak interactions with the neighboring segments of TMDs.

To ensure the *in vivo* role of these positively charged residues for the transport of WTA, we employed the so-called dominant negative method (27) to introduce mutant *tarG* into the strain *S. aureus* NCTC8325. Briefly, the wild-type and mutant *tarG* genes, both of which possess the native promoter of *tarG* and a region coding for the Flag tag at the N terminus, were introduced in *S. aureus* NCTC8325 using the shuttle plasmid pLI50. Western blotting against the antibody to Flag tag indicated the expression of the introduced TarG (Fig. S6C). The expressed TarG (both wild type and mutant) encoded by the plasmid could compete the original one encoded by the genome during the formation of ABC transporter TarGH. Single mutation of any of the four conserved positively charged residues, namely, Lys93, Arg98, Arg175, and Arg186, into either alanine or glutamate led to decrease of the WTA quantity at about 30% to 40%, compared to the wild type (Fig. 2C). Notably, we failed in obtaining the K93E mutant transformant, indicating that this mutation is most likely lethal to *S. aureus*. After data analysis, we found the mutation to glutamate generally displayed a more significant decrease of WTA yield than the corresponding mutation to alanine, which indicates the importance of the electrical property of these residues in the tunnel.

Scanning along the vertical path, we found a constrained bottleneck at the tunnel exit toward the extracellular space (Fig. 2B), which is guarded by Tyr51, Phe55, and Tyr190 from each TMD. The bottleneck has a radius of about 1.1 Å, which is unlikely to allow the water molecule to diffuse across the membrane through the transporter. It revealed that the present inward-open structure of TarGH possesses a closed exit of the substrate tunnel. Multiple-sequence alignment of TarG and homologs revealed that these three hydrophobic residues are highly conserved (Fig. S2C), indicating that these flippases might share a conserved bottleneck close to the substrate tunnel exit. Furthermore, we speculated that at the resting state, this bottleneck may prevent the diffusion of small molecules through the tunnel.

**Mapping the Targocil binding site on the TarGH structure.** The emergence of MRSA makes it an urgent necessity to develop a novel strategy different from the traditional therapeutic that uses antibiotics only. A recent report suggested that pretreatment with the WTA inhibitors could restore the  $\beta$ -lactam susceptibility of MRSA; thus, combined administration of medicines is capable of significantly reducing drug resistance (28). As a rate-limiting enzyme responsible for the last step of the WTA biosynthesis pathway, *S. aureus* TarGH was proposed to be a promising target of WTA inhibitors (4, 26). Indeed, a well-known inhibitor, termed Targocil, was chemically synthesized derived from a lead compound against MRSA (15). Moreover, sequence analysis of the Targocil-resistant *S. aureus* strains identified seven putative residues of TarGH involved in binding to Targocil (16). Thanks to the high sequence identity, five out of these seven Targocil-resistant residues of *S. aureus* TarGH could be eventually mapped on our present *A. herbarius* TarGH structure (Fig. 3A). Remarkably, four of these residues, Phe55, Trp73, Phe82, and Tyr190, on each TMD form a hydrophobic pocket (Fig. 3A), which is occupied by the loop between TM5 and EH1 that harbors another Targocil-resistant residue, Leu195. In addition, the pocket-forming residues Tyr190 and Phe55 also constitute one side of the bottleneck close to the tunnel exit (Fig. 2B), indicating a direct cross talk between this hydrophobic pocket and the bottleneck.

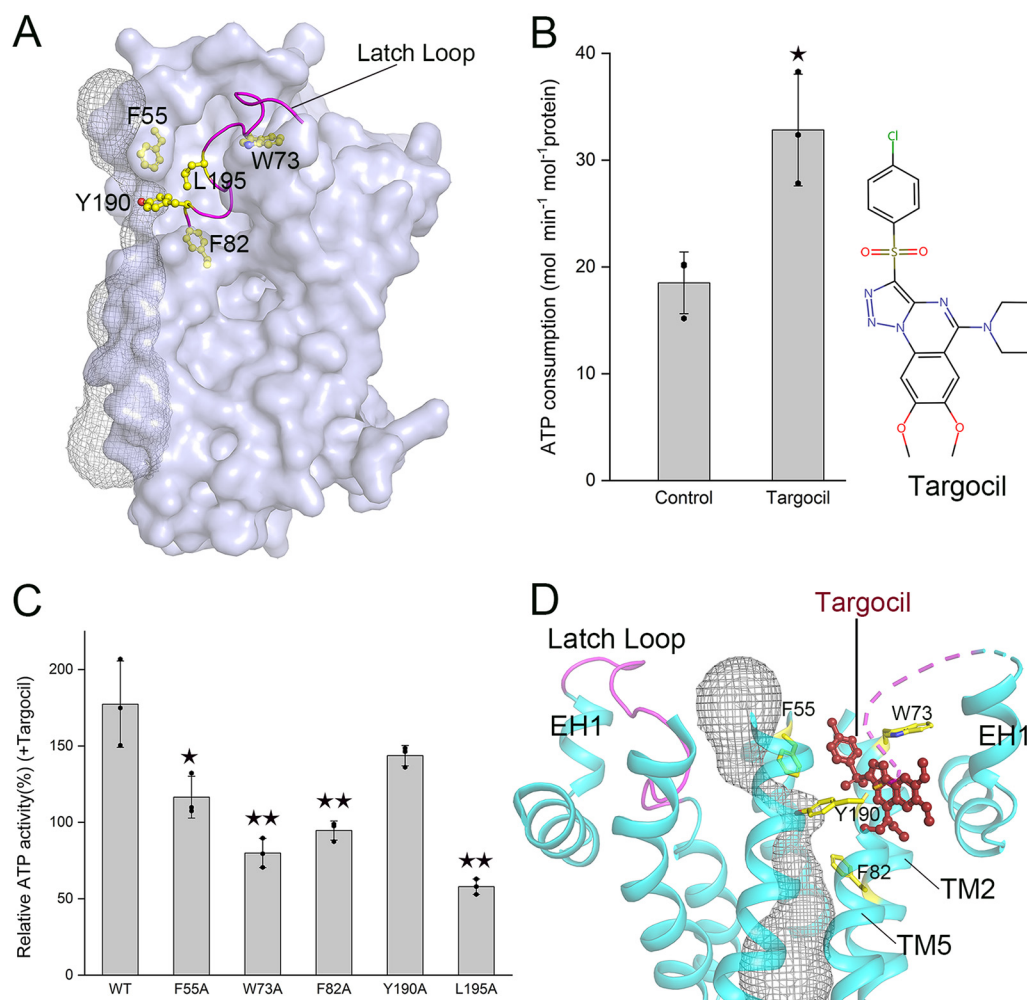


**FIG 3** The binding site of Targocil. (A) Five conserved Targocil-resistant residues (F55, W73, F82, Y190, and L195) are shown as yellow sticks, and the latch loop is shown in magenta. (B) ATPase activity of wild-type TarGH in the absence or presence of Targocil. (C) Relative ATPase activity of wild-type (WT) TarGH and mutants in the presence of Targocil. At least three independent experiments were performed for each assay of panels B and C. The means and standard deviations were calculated, and the data are presented as means  $\pm$  standard deviations. Two results of three experiments in the control group of panel B were overlapped due to similar values. Two-tailed Student's *t* test is used for the comparison of statistical significance. The *P* values of  $<0.05$ ,  $0.01$ , and  $0.001$  are indicated with single, double, and triple stars, respectively. (D) A docking model of Targocil on TarGH. The four Targocil-resistant residues F55, W73, F82, and Y190 flanking the bottleneck of the exit are shown in yellow.

Hence, we chemically synthesized Targocil, the structure of which was further proved by the nuclear magnetic resonance spectrum (Fig. S6A). According to the previously reported MIC (15), Targocil at a  $1 \mu\text{M}$  final concentration was applied to the ATPase activity assays of TarGH reconstituted in liposomes. In the absence and presence of Targocil, TarGH possesses a  $V_{\text{max}}$  of ATPase activity of  $18.5$  and  $32.8 \text{ mol min}^{-1} \text{ mol}^{-1} \text{ protein}$ , respectively (Fig. 3B). A significant increase of ATPase activity upon the addition of Targocil indicated that Targocil indeed specifically binds to TarGH. We speculated that conformational changes induced by the inhibitor may facilitate TarGH to adopt a conformation with elevated ATPase activity, in agreement with a recent report on human ABCB1, which gains an enhanced ATPase activity upon the addition of inhibitors (29).

To further precisely determine the binding site of Targocil, we sequentially mutated the five residues which were previously identified in *S. aureus* TarGH and conserved in *A. herbarius* TarGH. As predicted, except for Y190A, single mutation of any one of the other four Targocil-resistant residues resulted in a much less significant change of

TarGH ATPase activity upon the addition of Targocil (Fig. 3C). These results not only confirmed the previously identified Targocil-resistant residues (16) but also provided the direct biochemical and structural evidence that these residues are involved in Targocil binding.

Based on our ATPase activity assays in the presence of Targocil, we can constrain the possible binding site within a limited space. Notably, Targocil and the loop between TM5 and EH1 most likely exclusively bind to the hydrophobic pocket composed of Targocil-resistant residues; thus, we suspected that it might be shifted out of the pocket upon Targocil binding, and we termed it the latch loop. Indeed, once the latch loop was removed, Targocil could be well docked to the empty pocket using AutoDock Vina (30), at a lowest binding affinity energy of  $-8.1 \text{ kcal mol}^{-1}$  (Fig. 3D and Fig. S6D). Notably, two of the binding residues in our docking model, Phe55 and Tyr190, in addition to Leu195 on the latch loop (Fig. 3A), are exactly flanking one side of the bottleneck (Fig. 3D). It suggested that the tunnel exit is most likely restrained upon the inhibitor binding, leading to a decreased yield of WTA. In other words, the latch loop, which mimics the inhibitor, is also involved in the regulation of the opening and closing of the bottleneck. The results of ATPase activity assays in combination with the docking model enabled us to propose that Targocil serves as a wedge, which makes EH1, EH2, and TM6 shift outward, accompanying the inward shift of TM1 and TM5. Consequently, the tunnel becomes narrower, and meanwhile, the TMDs are slightly enlarged at the outward face, corresponding to the approach of the NBDs toward each other and a higher ATPase activity, in agreement with our results from activity assays (Movie S1).

**Structural comparison revealed a “crankshaft conrod” mechanism that amplifies the subtle conformational changes of TMDs.** Structural superposition using PyMol (<https://pymol.org/>) by the centers of molecules of our ATP-free TarGH against the Wzm-WztN structures in the ATP-free and ATP-bound forms gave a root mean square deviation (RMSD) of 4.7 Å over 832 C $\alpha$  atoms and 3.4 Å over 595 C $\alpha$  atoms, respectively. In addition, superposition of the TMDs yielded an RMSD of 3.9 Å over 375 C $\alpha$  atoms and 3.4 Å over 341 C $\alpha$  atoms, respectively. It suggested that our structure resembles the two structures of Wzm-WztN, which undergo subtle conformational changes upon ATP binding. Moreover, compared to the ATP-bound Wzm-WztN, fewer conformational changes could be observed in the overall structure of our ATP-free TarGH, except for a rigid-body rotation of the TMDs at about 15° (Fig. 4A and E). In contrast to the blocked tunnel at the bottleneck in our ATP-free structure, a pair of TM5 helices that constitute the wall of the substrate tunnel tilt away from each other, along with the corresponding latch loops flipping outward, resulting in opening of the tunnel in the structure of Wzm-WztN upon ATP binding (Fig. 4B), which eventually enables the substrate to be pumped out.

Structural comparison revealed that TarGH possesses an open tunnel entrance in the absence of ATP (Fig. 4C), compared to a closed entrance in the structure of ATP-bound Wzm-WztN (Fig. 4C). Due to the high flexibility of the gate loop (GL), the entrance of the substrate tunnel in TarGH is accessible. In contrast, the entrance in the structure of ATP-bound Wzm-WztN is closed due to the conformational changes at two loops, Loop<sub>IF-TM1</sub> and Loop<sub>TM4-TM5</sub>, in addition to the GH, which is folded most likely via interactions with the adjacent loops. A couple of interactions among the three segments were observed in ATP-bound Wzm-WztN (Fig. 4C), including the hydrogen bond of Gln18 from GH and Thr21 from Loop<sub>IF-TM1</sub>, in addition to hydrophobic and non-bonded contacts among the three segments, resulting in a closed entrance. Sequence analysis indicated that the GL possesses positively charged residues, such as Lys18, Arg19, and Arg23 in TarGH, and Loop<sub>TM4-TM5</sub> contains a very conserved Arg175-Asp176 motif (Fig. 4C and Fig. S2C). In addition, the conserved aspartate residue was proposed to be responsible for the binding of the diphosphate moiety of UND-PP (31, 32). Similarly, a substrate tunnel entrance clustering of positively charged residues in addition to a conserved aspartate residue, Asp167, could be found in Wzm-WztN (Fig. 4C). In fact, the WTA yield assays using the dominant negative method revealed



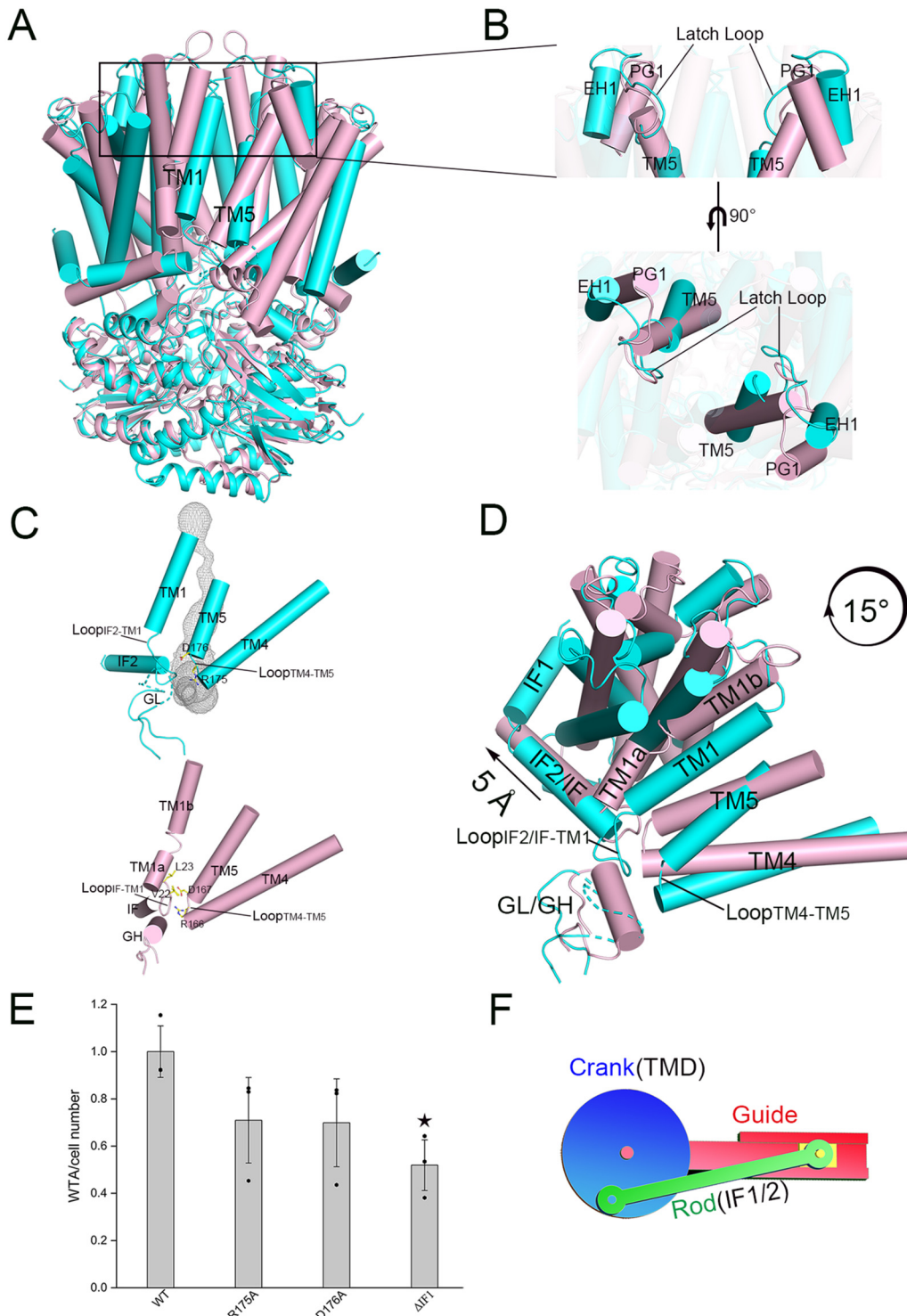


**FIG 4** Structural comparison. (A) Overall structure superposition of ATP-free TarGH on ATP-bound Wzm-WztN. (B) A close look at the latch loop region. (C) The entrance of the substrate tunnel in ATP-free TarGH and ATP-bound Wzm-WztN. (D) A top view of superimposed TMDs of ATP-free TarGH and ATP-bound Wzm-WztN. (E) Quantification of WTA in *S. aureus* NCTC8325 transformed with pLI50-*tarG* and its D-R motif mutants, as well as the IF1 truncation ( $\Delta$ IF1) version. At least three independent assays were performed. At least three independent experiments were performed for each assay. The means and standard deviations were calculated, and the data are presented as means  $\pm$  standard deviations. Two results of three experiments in the wild-type (WT) group were overlapped due to similar values. Two-tailed Student's *t* test is used for the comparison of statistical significance. The *P* values of  $<0.05$ , 0.01, and 0.001 are indicated with single, double, and triple stars, respectively. (F) A scheme of the crankshaft conrod and corresponding structural components. TarGH is shown in cyan, and Wzm-WztN is shown in pink. The corresponding structural segments including TM1, TM5, the latch loop, GL/GH, Loop<sub>IF-TM1</sub>, and Loop<sub>TM4-TM5</sub> are labeled.



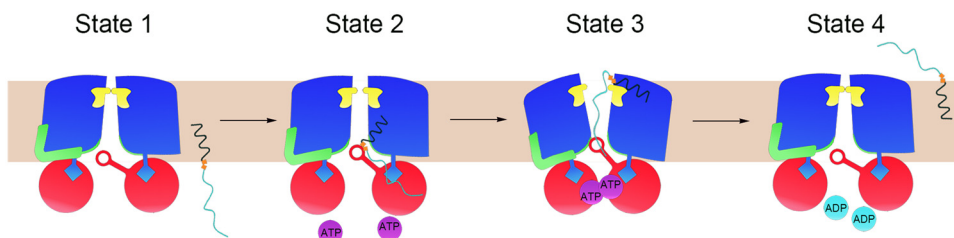


**FIG 5** A putative transport cycle. States 1, 2, 3, and 4 represent the resting state, substrate binding state, ATP binding state, and ATP hydrolyzed state after substrate translocation, respectively. The NBD, TMD, latch loop, and IF, and their corresponding loops, are colored in red, blue, yellow, and green, respectively. The coupling helix and gate loop are shown as a blue rectangle and a red circle protruding from the TMD and NBD, respectively. The substrate is shown as a curled line.

that mutation of either Arg175 or Asp176 to alanine somewhat impairs the WTA synthesis, leading to an  $\sim 30\%$  decrease of total WTA (Fig. 4E).

Despite the subtle changes of overall structure, along with the clockwise rotation of the TMD of ATP-bound Wzm-WztN against that of TarGH, the interface helix IF that sticks on the TMD undergoes a horizontal translation of about 5 Å. In consequence, the loop succeeding the IF, namely, Loop<sub>IF-TM1</sub>, shifts the tunnel entrance inward, along with the approach of GH toward Loop<sub>TM4-TM5</sub> (Fig. 4D). It suggested that the subtle conformational changes of TMDs could be transmitted and amplified by the IF, which triggers a rather significant conformational change of the tunnel entrance. This transformation of the force is reminiscent of the mechanical device the crankshaft conrod (Movie S2). In the present case, the TMD mimics the crank, whereas the IF resembles the rod (Fig. 4F). To compensate for the fewer conformational changes upon ATP binding, TarGH possesses an extra interface helix IF1 at the N terminus, in addition to IF2, which corresponds to the IF of Wzm-WztN. As predicted, truncation of IF1 resulted in a significant reduction of WTA yield to about 50%, compared to the wild type (Fig. 4E). Altogether, TarGH adopts a crankshaft conrod mechanism to pump out a relatively big substrate through subtle conformational changes along the NBDs and TMDs.

## DISCUSSION

The present structure of TarGH, in combination with previous studies (19, 23, 24, 33–35), enabled us to propose a crankshaft conrod-aided transport cycle for type II exporters (Fig. 5). The ATP-free TarGH adopts a resting state, with the substrate tunnel closed at the exit and open at the entrance (Fig. 5, state 1), as shown in our cryo-EM structure. At this state, the latch loop blocks the exit and functions as an autoinhibitor that mimics the exogenous inhibitor Targocil, while the entrance formed by the GL and Loop<sub>TM4-TM5</sub> is open and ready for substrate recognition and binding. At the initial step, the diphosphate group of the UND-PP moiety could be first recognized by the conserved D-R motif at the entrance, which further guides the approaching substrate (Fig. 5, state 2). Upon binding to ATP, NBDs move toward each other, making TMDs adopt an outward-open conformation (Fig. 5, state 3). In this transition process, the rigid-body rotation of each TMD is transformed to a horizontal translation of the IFs through the crankshaft conrod mechanism. Along with the backward movement of the IFs, the succeeding Loop<sub>IF2-TM1</sub> bends the TMD inward. In consequence, Loop<sub>TM4-TM5</sub> and GL are recruited via hydrophobic and hydrophilic interactions to form a closed entrance, which might facilitate the insertion of the sugar moiety to the transmembrane tunnel. However, whether the UND moiety is translocated inside or outside the tunnel remains unknown, although it was previously proposed to stay in the membrane bilayer without entering the TMDs in the cases of Pglk and Wzm-Wzt (18, 20). Meanwhile, latch loops are ejected and the tunnel exit opens toward the extracellular space. At the final step, ATP is hydrolyzed by the dimerized NBDs, the energy of which drives the translocation of the substrate and eventually makes TarGH go back to the resting state (Fig. 5, state 4). As previously proposed (20), the UND moiety most likely continues

inserting in the outer leaflet of the membrane whereas the diphosphate group and sugar moiety are exposed to the extracellular space. Notably, it might take several cycles of transport to pump out one molecule of UND-PP-linked oligosaccharide.

In contrast to type I exporters, conformational changes in type II exporters are relatively subtle. How such subtle conformational changes can accomplish the transport of a large substrate remains unknown. Our present cryo-EM structure combined with the previously reported Wzm-WztN crystal structures provided insights into the transformation of the chemical energy of ATP hydrolysis to rigid-body rotation of TMDs, which is further amplified by a crankshaft conrod mechanism to the horizontal translation of the interface helices. This hypothesis can be applied to most ABC exporters possessing similar structural components.

## MATERIALS AND METHODS

**Protein preparation.** The codon-optimized *tarG* and *tarH* genes were synthesized by Sangon Biotech. *tarG* and *tarH* genes were cloned into a single modified pET-19b vector (YouBio) by using the One Step Cloning kit (Vazyme), with the *tarG* product containing an N-terminal decahistidine tag. The plasmid was transformed into the *Escherichia coli* BL21(DE3) strain (Invitrogen), growing at 37°C in lysogeny broth (LB) culture medium, supplemented with 50 µg ml<sup>-1</sup> ampicillin. Overexpression of TarGH was induced by adding 0.2 mM IPTG (isopropyl-β-D-thiogalactopyranoside) (Biofroxx) when the cell density reached an optical density at 600 nm (OD<sub>600</sub>) of 0.6 to 0.8. At 4 h after induction at 37°C, cells were collected by centrifugation; homogenized in buffer containing 50 mM Tris-HCl (pH 7.5), 500 mM NaCl, 7 mM β-mercaptoethanol (β-ME) plus 10% glycerol; and stored at -80°C before use.

For purification, cells were thawed followed by disruption with a Constant cell disruption system (Constant Systems) with two passes at 30 kpsi. Cell debris was removed by low-speed centrifugation for 15 min. The supernatant was collected and ultracentrifuged at 200,000 × *g* for 1 h. The membrane fraction was collected and incubated for 1.5 h with buffer containing 50 mM Tris-HCl (pH 7.5), 500 mM NaCl, 7 mM β-ME, 10% glycerol, 1% (wt/vol) dodecyl-β-D-maltopyranoside (DDM; Anatrace), and 1% (wt/vol) octaethylene glycol monododecyl ether (C<sub>12</sub>E<sub>8</sub>; Anatrace) at 4°C. After another round of ultracentrifugation at 200,000 × *g* for 30 min, the supernatant was collected and loaded onto nickel affinity resin (nickel-nitrilotriacetic acid [Ni-NTA]; Qiagen). The column was then washed with 50 mM Tris-HCl (pH 7.5), 500 mM NaCl, 7 mM β-ME, 10% glycerol, and 0.04% DDM. Contaminants were removed by washing with 50 mM Tris (pH 7.5), 500 mM NaCl, 7 mM β-ME, 10% glycerol, and 0.04% DDM plus 20 mM imidazole and 40 mM imidazole successively. Protein was eluted from the affinity resin with buffer containing 50 mM Tris (pH 7.5), 500 mM NaCl, 7 mM β-ME, 10% glycerol, 0.04% DDM, and 400 mM imidazole. Afterward, the eluent was concentrated to 2 ml before further purification by gel filtration (Superdex 200 increase 10/300; GE Healthcare) in the buffer containing 50 mM Tris-HCl (pH 7.5), 500 mM NaCl, 7 mM β-ME, 10% glycerol, and 0.03% *n*-undecyl-β-D-maltopyranoside (UDM; Anatrace). Peak fractions were pooled, and desalting was implemented with buffer containing 20 mM Tris-HCl (pH 7.5), 100 mM NaCl, 7 mM β-ME, 10% glycerol, and 0.03% UDM. Then, it was concentrated for EM analysis.

The mutated plasmid pET19b-*tarGH* (*tarH*<sub>E169Q</sub>) was also constructed by using the One Step Cloning kit (Vazyme). The mutated protein purification was the same as the wild type.

**Sample preparation and cryo-EM data acquisition.** Purified TarGH<sub>E169Q</sub> was concentrated to 8 mg ml<sup>-1</sup> for cryo-EM sample preparation implemented with FEI Vitrobot Mark IV. A 3.5-µl amount of protein was applied to a glow-discharged Quantifoil holey carbon grid (1.2/1.3, 300 mesh). Grids were blotted for 4 s with 100% humidity and plunge-frozen in liquid ethane.

Cryo-EM data were collected at liquid nitrogen temperature on a Titan Krios transmission electron microscope (FEI), operating at 300 kV and equipped with a K2 Summit direct electron detector (Gatan) and a Gatan GIF quantum energy filter (slit width, 15 eV). A total of 4,985 micrograph stacks were automatically collected with SerialEM (36) at a nominal magnification of ×59,000 with a defocus range of -1.5 to -2.5 µm, which yielded a final pixel size of 1.36 Å. Each stack was exposed for 8 s with an exposure time of 0.25 s per frame, resulting in 32 frames per stack. The total dose rate was about 64 e<sup>-</sup>/Å<sup>2</sup> for each stack.

**Image processing.** A simplified flow chart for the image processing procedure is presented in Fig. S4. The motion-corrected, dose-weighted 4,985 micrographs collected from the Institute of Biophysics, Chinese Academy of Sciences, were imported in Relion 2.0 (37). A total of 4,185 micrograph stacks were manually picked for further data processing. To generate a template for automatic particle picking, approximately 2,000 particles were manually picked. A total of 893,306 particles were picked from 4,185 electron micrographs automatically. After two-dimensional (2D) classification, 509,711 particles were selected and subjected to a global angular search three-dimensional (3D) classification. The initial model was generated with images of selected 2D class averages. A total of 305,822 good particles were selected from the local angular search 3D classification and merged together. These particles were then subjected to a local angular search 3D autorefinement, resulting in a 3D reconstruction map with a resolution of 4.18 Å after postprocessing. A guided multireference 3D classification procedure was then applied to the merged data set using Relion 2.0. Particles of the best-classified class were subjected to 3D autorefinement, resulting in a 3D reconstruction map with a resolution of 4.05 Å after postprocessing. A soft overall mask was generated from one of the two unfiltered half-reconstruction maps with a suitable initial binarization threshold using Relion 2.0. The map quality was improved when the particles were subjected

to 3D autorefinement with the soft overall mask applied, and the resolution of the reconstruction map after postprocessing reached 3.94 Å. The resolution was estimated with the gold-standard FSC 0.143 criterion (38) with a high-resolution noise substitution method. Local resolution variations were estimated using ResMap (39).

**Model building and refinement.** The overall TarGH map at 3.9 Å was used for *de novo* model building. An all-alanine model was first built manually in Coot (40). Based on the structural alignment between TarGH and homolog Wzm/WztN (PDB code 6OIH), the main TMs were built by homology modeling. The side chains were assigned mainly by bulky residues such as Arg, Phe, Tyr, and Trp. High homology existed between WztN and TarH, so the structure of the WztN of Wzm/WztN was docked into the map and manually adjusted in Coot.

The model was further improved by iterative refinement in real space with secondary structure and geometry restraints using Phenix (41), rebuilt in Coot, and evaluated by MolProbity (42, 43). The structure figures were prepared using the program CHIMERA (44) or PyMOL. Statistics on the 3D reconstruction and model refinement can be found in Table S1.

**ATPase activity assays.** All ATP hydrolysis assays were performed in the proteoliposomes. *E. coli* polar lipids (Avanti) were resuspended in 20 mM HEPES-KOH (pH 7.0) to the final concentration of 20 mg ml<sup>-1</sup>. A 0.45% final concentration of Triton X-100 was added to destabilize the liposomes for 0.5 h at room temperature. The proteins were added to the destabilized liposomes and incubated for 1 h at 4°C. The ratio of lipids and proteins was kept at 100:1 (wt/wt). Triton X-100 was removed by SM-2 adsorbent biobeads (Bio-Rad) by incubation at 4°C overnight and repeated for another 2 h. Proteoliposomes were diluted and resuspended twice with the ice-cold buffer at 250,000 × *g* for 1 h at 4°C. After the final centrifugation, the pellets were resuspended in 20 mM HEPES-KOH (pH 7.0), 50 mM KCl, and 2 mM MgCl<sub>2</sub> to 100 μl as one reaction sample. For each reaction sample, 0.1 μM TarGH was added.

Targocil was first solubilized in dimethyl sulfoxide (DMSO) to 10 mM and then diluted to 100 μM with double-distilled water (ddH<sub>2</sub>O). For each 100-μl reaction sample, 1 μM Targocil was added, indicating that 0.01% DMSO was included. Thus, we added equal amounts of DMSO as supplements for control groups. Afterward, ATP was added to each sample at a final concentration of 2 mM by three rounds of freezing in liquid nitrogen followed by thawing in a bath sonicator. Reactions were performed at 37°C for 1 h, and the amount of released phosphate ion was quantitatively measured using the ATPase colorimetric assay kit (Innova Biosciences) in 96-well plates at OD<sub>650</sub>.

**Targocil docking on TarGH.** To dock Targocil on our TarGH structure, the latch loop was removed for one symmetry unit by editing the PDB file, as the latch loop has occupied the putative pocket where Targocil most likely binds, based on the previously reported mutation screening and our biochemical assays. Targocil was set as “ligand,” and the edited PDB file was set as “receptor.” We determined the coordinate of the docking space in AutoDock Vina as (128.435, 140.345, 110.712), and the size of the space for the docking was restrained as a 16.0- by 28.0- by 18.0-Å<sup>3</sup> box. The “exhaustiveness” for the calculation was set to 1,000. The output of the docking produced 9 models, with an affinity from -7.5 to -8.1 kcal/mol. The model with the lowest binding affinity energy is shown in Fig. 3D, and all nine models are displayed with different colors for one symmetric unit in Fig. S6D.

**Dominant negative method to introduce mutant TarGH into *S. aureus* NCTC8325.** The gene fragment encompassing *tarG* and its native promoter were amplified from *S. aureus* NCTC8325 genomic DNA. The fragment was cloned into the shuttle plasmid pLI50, and a Flag tag was added at the N-terminal part of the gene product to derive the plasmid pLI50-*tarG*. This plasmid pLI50 with the N-terminal Flag tag was constructed by using the One Step Cloning kit (Vazyme). The mutated pLI50-*tarG* mentioned in this paper was constructed by using the One Step Cloning kit (Vazyme). The wild-type *tarG* and *tarG* mutant plasmids were transformed by electroporation into *S. aureus* strain RN4220 for modification and subsequently into *S. aureus* NCTC8325.

**Purification of the recombinant expressed TarG from *S. aureus* NCTC8325.** The pLI50-*tarG*-transformed *S. aureus* NCTC8325 was cultured at 37°C in 400 ml tryptic soy broth (TSB) culture medium overnight, supplemented with 17 μg ml<sup>-1</sup> chloramphenicol. Then, the cells were collected by centrifugation; homogenized in buffer containing 50 mM Tris-HCl (pH 7.5), 500 mM NaCl, and 2 mM dithiothreitol plus 10% glycerol; and stored at -80°C if not for immediate use.

The cells were disrupted with a Constant cell disruption system (Constant Systems) with one pass at 30 kpsi. Cell debris was removed by centrifugation at 12,000 × *g* for 30 min. The supernatant was collected and incubated with the anti-Flag M2 affinity gel (Sigma) on ice for 1 h. Then, the resin was loaded onto the column and washed with 5 ml of wash buffer containing 50 mM Tris-HCl (pH 7.5), 500 mM NaCl, 10% (wt/wt) glycerol, and 0.04% (wt/wt) DDM. Protein was eluted with 6 ml of wash buffer plus 200 μg ml<sup>-1</sup> Flag peptide. Subsequently, the protein was used for Western blotting assay. Flag tag antibody (catalog number 66008-3-Ig) was purchased from Proteintech.

**Extraction and quantification of *S. aureus* WTA.** Each portion of WTA was extracted from 10 ml of the *S. aureus* NCTC8325 strain cultured overnight. The extraction method strictly followed the protocol of the work of Covas et al. (45). The quantification of WTA was applied by the measure of the phosphate group from WTA using the ATPase colorimetric assay kit (Innova Biosciences) in 96-well plates at OD<sub>650</sub>.

**Data availability.** The accession number of our structure in PDB is 6JBH and in EMD is EMD-9790.

## SUPPLEMENTAL MATERIAL

Supplemental material is available online only.

**FIG S1**, TIF file, 2.9 MB.

**FIG S2**, TIF file, 2.8 MB.

**FIG S3**, TIF file, 2.8 MB.

**FIG S4**, TIF file, 2.7 MB.

**FIG S5**, TIF file, 1.8 MB.

**FIG S6**, TIF file, 2.3 MB.

**TABLE S1**, DOCX file, 0.02 MB.

**MOVIE S1**, AVI file, 0.9 MB.

**MOVIE S2**, AVI file, 1.5 MB.

## ACKNOWLEDGMENTS

We thank Xiaojun Huang and Boling Zhu at the Center for Biological Imaging, Core Facilities for Protein Science, at the Institute of Biophysics (IBP), Chinese Academy of Sciences, for technical support during cryo-EM image acquisition; Peiping Tang at the Center for Integrative Imaging, Hefei National Laboratory for Physical Sciences at the Microscale, University of Science and Technology of China, for cryo-EM sample examination; and Liuzhu Gong at the School of Chemistry and Materials Science, University of Science and Technology of China, for help in Targocil synthesis.

This work is supported by the Ministry of Science and Technology of China (<http://www.most.gov.cn>, grants 2019YFA0508500 and 2015CB910103), the Chinese Academy of Science (grant no. XDB08020304), the National Foundation of Natural Science of China (<http://www.most.gov.cn>, grants 31621002 and 31600599), and the Fundamental Research Funds for the Central Universities (grant no. YD2070002005).

Y.C. and C.-Z.Z. conceived, designed, and supervised the project. L.C., W.-T.H., and L.S. designed and performed the experiments. C.-Z.Z., Y.C., L.C., and W.-T.H. analyzed data and wrote the manuscript. All authors discussed the data and read the manuscript.

The authors declare no competing interests.

## REFERENCES

- Weidenmaier C, Kokai-Kun JF, Kristian SA, Chanturiya T, Kalbacher H, Gross M, Nicholson G, Neumeister B, Mond JJ, Peschel A. 2004. Role of teichoic acids in *Staphylococcus aureus* nasal colonization, a major risk factor in nosocomial infections. *Nat Med* 10:243–245. <https://doi.org/10.1038/nm991>.
- Chambers HF, DeLeo FR. 2009. Waves of resistance: *Staphylococcus aureus* in the antibiotic era. *Nat Rev Microbiol* 7:629–641. <https://doi.org/10.1038/nrmicro2200>.
- Bagnoli F, Rappuoli R (ed). 2017. Current topics in microbiology and immunology, vol 404. Protein and sugar export and assembly in Gram-positive bacteria. Springer, Cham, Switzerland.
- Brown S, Santa Maria JP, Jr, Walker S. 2013. Wall teichoic acids of Gram-positive bacteria. *Annu Rev Microbiol* 67:313–336. <https://doi.org/10.1146/annurev-micro-092412-155620>.
- Ellwood D. 1970. The wall content and composition of *Bacillus subtilis* var. niger grown in a chemostat. *Biochem J* 118:367–373. <https://doi.org/10.1042/bj1180367>.
- Tomita S, Irisawa T, Tanaka N, Nukada T, Satoh E, Uchimura T, Okada S. 2010. Comparison of components and synthesis genes of cell wall teichoic acid among *Lactobacillus plantarum* strains. *Biosci Biotechnol Biochem* 74:928–933. <https://doi.org/10.1271/bbb.90736>.
- Weidenmaier C, Peschel A, Xiong Y-Q, Kristian SA, Dietz K, Yeaman MR, Bayer AS. 2005. Lack of wall teichoic acids in *Staphylococcus aureus* leads to reduced interactions with endothelial cells and to attenuated virulence in a rabbit model of endocarditis. *J Infect Dis* 191:1771–1777. <https://doi.org/10.1086/429692>.
- Gerlach D, Guo Y, De Castro C, Kim S-H, Schlatterer K, Xu F-F, Pereira C, Seeberger PH, Ali S, Codée J, Sirisarn W, Schulte B, Wolz C, Larsen J, Molinaro A, Lee BL, Xia G, Stehle T, Peschel A. 2018. Methicillin-resistant *Staphylococcus aureus* alters cell wall glycosylation to evade immunity. *Nature* 563:705–709. <https://doi.org/10.1038/s41586-018-0730-x>.
- Bera A, Biswas R, Herbert S, Kulauzovic E, Weidenmaier C, Peschel A, Götz F. 2007. Influence of wall teichoic acid on lysozyme resistance in *Staphylococcus aureus*. *J Bacteriol* 189:280–283. <https://doi.org/10.1128/JB.01221-06>.
- Brown S, Zhang Y-H, Walker S. 2008. A revised pathway proposed for *Staphylococcus aureus* wall teichoic acid biosynthesis based on in vitro reconstitution of the intracellular steps. *Chem Biol* 15:12–21. <https://doi.org/10.1016/j.chembiol.2007.11.011>.
- Raetz CR, Whitfield C. 2002. Lipopolysaccharide endotoxins. *Annu Rev Biochem* 71:635–700. <https://doi.org/10.1146/annurev.biochem.71.110601.135414>.
- Van Heijenoort J. 2001. Recent advances in the formation of the bacterial peptidoglycan monomer unit. *Nat Prod Rep* 18:503–519. <https://doi.org/10.1039/a804532a>.
- Yother J. 2011. Capsules of *Streptococcus pneumoniae* and other bacteria: paradigms for polysaccharide biosynthesis and regulation. *Annu Rev Microbiol* 65:563–581. <https://doi.org/10.1146/annurev.micro.62.081307.162944>.
- Sanyal S, Menon AK. 2009. Flipping lipids: why an' what's the reason for? *ACS Chem Biol* 4:895–909. <https://doi.org/10.1021/cb900163d>.
- Lee K, Campbell J, Swoboda JG, Cuny GD, Walker S. 2010. Development of improved inhibitors of wall teichoic acid biosynthesis with potent activity against *Staphylococcus aureus*. *Bioorg Med Chem Lett* 20:1767–1770. <https://doi.org/10.1016/j.bmcl.2010.01.036>.
- Schirner K, Stone LK, Walker S. 2011. ABC transporters required for export of wall teichoic acids do not discriminate between different main chain polymers. *ACS Chem Biol* 6:407–412. <https://doi.org/10.1021/cb100390w>.
- Young NM, Brisson J-R, Kelly J, Watson DC, Tessier L, Lanthier PH, Jarrell HC, Cadotte N, St Michael F, Aberg E, Szymanski CM. 2002. Structure of the N-linked glycan present on multiple glycoproteins in the Gram-negative bacterium, *Campylobacter jejuni*. *J Biol Chem* 277:42530–42539. <https://doi.org/10.1074/jbc.M206114200>.
- Perez C, Gerber S, Boilevin J, Bucher M, Darbre T, Aebi M, Reymond JL, Locher KP. 2015. Structure and mechanism of an active lipid-linked oligosaccharide flippase. *Nature* 524:433–438. <https://doi.org/10.1038/nature14953>.
- Bi Y, Mann E, Whitfield C, Zimmer J. 2018. Architecture of a channel-forming O-antigen polysaccharide ABC transporter. *Nature* 553:361–365. <https://doi.org/10.1038/nature25190>.
- Caffalette CA, Corey RA, Sansom MSP, Stansfeld PJ, Zimmer J. 2019. A lipid gating mechanism for the channel-forming O antigen ABC transporter. *Nat Commun* 10:824. <https://doi.org/10.1038/s41467-019-08646-8>.



21. Mann E, Mallette E, Clarke BR, Kimber MS, Whitfield C. 2016. The *Klebsiella pneumoniae* O12 ATP-binding cassette (ABC) transporter recognizes the terminal residue of its O-antigen polysaccharide substrate. *J Biol Chem* 291:9748–9761. <https://doi.org/10.1074/jbc.M116.719344>.
22. Cuthbertson L, Powers J, Whitfield C. 2005. The C-terminal domain of the nucleotide-binding domain protein Wzt determines substrate specificity in the ATP-binding cassette transporter for the lipopolysaccharide O-antigens in *Escherichia coli* serotypes O8 and O9a. *J Biol Chem* 280:30310–30319. <https://doi.org/10.1074/jbc.M504371200>.
23. Qian H, Zhao X, Cao P, Lei J, Yan N, Gong X. 2017. Structure of the human lipid exporter ABCA1. *Cell* 169:1228–1239.e10. <https://doi.org/10.1016/j.cell.2017.05.020>.
24. Lee J-Y, Kinch LN, Borek DM, Wang J, Wang J, Urbatsch IL, Xie X-S, Grishin NV, Cohen JC, Otwinowski Z, Hobbs HH, Rosenbaum DM. 2016. Crystal structure of the human sterol transporter ABCG5/ABCG8. *Nature* 533:561–564. <https://doi.org/10.1038/nature17666>.
25. Chovancova E, Pavelka A, Benes P, Strnad O, Brezovsky J, Kozlikova B, Gora A, Sustr V, Klvana M, Medek P, Biedermannova L, Sochor J, Damborsky J. 2012. CAVER 3.0: a tool for the analysis of transport pathways in dynamic protein structures. *PLoS Comput Biol* 8:e1002708. <https://doi.org/10.1371/journal.pcbi.1002708>.
26. Swoboda JG, Meredith TC, Campbell J, Brown S, Suzuki T, Bollenbach T, Malhowski AJ, Kishony R, Gilmore MS, Walker S. 2009. Discovery of a small molecule that blocks wall teichoic acid biosynthesis in *Staphylococcus aureus*. *ACS Chem Biol* 4:875–883. <https://doi.org/10.1021/cb900151k>.
27. Herskowitz I. 1987. Functional inactivation of genes by dominant negative mutations. *Nature* 329:219–222. <https://doi.org/10.1038/329219a0>.
28. Wang H, Gill CJ, Lee SH, Mann P, Zuck P, Meredith TC, Murgolo N, She X, Kales S, Liang L, Liu J, Wu J, Santa Maria J, Su J, Pan J, Hailey J, McGuinness D, Tan CM, Flattery A, Walker S, Black T, Roemer T. 2013. Discovery of wall teichoic acid inhibitors as potential anti-MRSA  $\beta$ -lactam combination agents. *Chem Biol* 20:272–284. <https://doi.org/10.1016/j.chembiol.2012.11.013>.
29. Dastvan R, Mishra S, Peskova YB, Nakamoto RK, McHaourab HS. 2019. Mechanism of allosteric modulation of P-glycoprotein by transport substrates and inhibitors. *Science* 364:689–692. <https://doi.org/10.1126/science.aav9406>.
30. Trott O, Olson AJ. 2010. AutoDock Vina: improving the speed and accuracy of docking with a new scoring function, efficient optimization, and multithreading. *J Comput Chem* 31:455–461. <https://doi.org/10.1002/jcc.21334>.
31. Manat G, Roure S, Auger R, Bouhss A, Barretheau H, Mengin-Lecreux D, Touzé T. 2014. Deciphering the metabolism of undecaprenyl-phosphate: the bacterial cell-wall unit carrier at the membrane frontier. *Microb Drug Resist* 20:199–214. <https://doi.org/10.1089/mdr.2014.0035>.
32. Petrou VI, Herrera CM, Schultz KM, Clarke OB, Vendome J, Tomasek D, Banerjee S, Rajashankar KR, Dufresne MB, Kloss B, Kloppmann E, Rost B, Klug CS, Trent MS, Shapiro L, Mancia F. 2016. Structures of aminoarabinose transferase ArnT suggest a molecular basis for lipid A glycosylation. *Science* 351:608–612. <https://doi.org/10.1126/science.aad1172>.
33. Beis K. 2015. Structural basis for the mechanism of ABC transporters. *Biochem Soc Trans* 43:889–893. <https://doi.org/10.1042/BST20150047>.
34. Locher KP. 2016. Mechanistic diversity in ATP-binding cassette (ABC) transporters. *Nat Struct Mol Biol* 23:487–493. <https://doi.org/10.1038/nsmb.3216>.
35. Ter Beek J, Guskov A, Slotboom DJ. 2014. Structural diversity of ABC transporters. *J Gen Physiol* 143:419–435. <https://doi.org/10.1085/jgp.201411164>.
36. Mastrorade DN. 2005. Automated electron microscope tomography using robust prediction of specimen movements. *J Struct Biol* 152:36–51. <https://doi.org/10.1016/j.jsb.2005.07.007>.
37. Scheres S. 2012. A Bayesian view on cryo-EM structure determination. *J Mol Biol* 415:406–418. <https://doi.org/10.1016/j.jmb.2011.11.010>.
38. Rosenthal PB, Henderson R. 2003. Optimal determination of particle orientation, absolute hand, and contrast loss in single-particle electron cryomicroscopy. *J Mol Biol* 333:721–745. <https://doi.org/10.1016/j.jmb.2003.07.013>.
39. Kucukelbir A, Sigworth FJ, Tagare HD. 2014. Quantifying the local resolution of cryo-EM density maps. *Nat Methods* 11:63–65. <https://doi.org/10.1038/nmeth.2727>.
40. Emsley P, Cowtan K. 2004. Coot: model-building tools for molecular graphics. *Acta Crystallogr D Biol Crystallogr* 60:2126–2132. <https://doi.org/10.1107/S0907444904019158>.
41. Adams PD, Afonine PV, Bunkóczi G, Chen VB, Davis IW, Echols N, Headd JJ, Hung L-W, Kapral GJ, Grosse-Kunstleve RW, McCoy AJ, Moriarty NW, Oeffner R, Read RJ, Richardson DC, Richardson JS, Terwilliger TC, Zwart PH. 2010. PHENIX: a comprehensive Python-based system for macromolecular structure solution. *Acta Crystallogr D Biol Crystallogr* 66:213–221. <https://doi.org/10.1107/S0907444909052925>.
42. Davis IW, Leaver-Fay A, Chen VB, Block JN, Kapral GJ, Wang X, Murray LW, Arendall WB, Snoeyink J, Richardson JS, Richardson DC. 2007. MolProbity: all-atom contacts and structure validation for proteins and nucleic acids. *Nucleic Acids Res* 35:W375–W383. <https://doi.org/10.1093/nar/gkm216>.
43. Chen VB, Arendall WB, Headd JJ, Keedy DA, Immormino RM, Kapral GJ, Murray LW, Richardson JS, Richardson DC. 2010. MolProbity: all-atom structure validation for macromolecular crystallography. *Acta Crystallogr D Biol Crystallogr* 66:12–21. <https://doi.org/10.1107/S0907444909042073>.
44. Pettersen EF, Goddard TD, Huang CC, Couch GS, Greenblatt DM, Meng EC, Ferrin TE. 2004. UCSF Chimera—a visualization system for exploratory research and analysis. *J Comput Chem* 25:1605–1612. <https://doi.org/10.1002/jcc.20084>.
45. Covas G, Vaz F, Henriques G, Pinho MG, Filipe SR. 2016. Analysis of cell wall teichoic acids in *Staphylococcus aureus*. *Methods Mol Biol* 1440:201–213. [https://doi.org/10.1007/978-1-4939-3676-2\\_15](https://doi.org/10.1007/978-1-4939-3676-2_15).